Journal of Computational Neuroscience 6, 5–26 (1999)

Signals in Stochastically Generated Neurons

JAMES L. WINSLOW AND STEPHAN F. JOU
Physiology Department and Institute of Biomedical Engineering, University of Toronto, Toronto, Ont. M5S 1A8
winslow@spine.med.utoronto.ca

SABRINA WANG AND J. MARTIN WOJTOWICZ
Physiology Department, University of Toronto, Toronto, Ont. M5S 1A8

Received July 10, 1997; Revised February 10, 1998; Accepted February 17, 1998

Action Editor:

Abstract. To incorporate variation of neuron shape in neural models, we developed a method of generating a population of realistically shaped neurons. Parameters that characterize a neuron include soma diameters, distances to branch points, fiber diameters, and overall dendritic tree shape and size. Experimentally measured distributions provide a means of treating these morphological parameters as stochastic variables in an algorithm for production of neurons. Stochastically generated neurons shapes were used in a model of hippocampal dentate gyrus granule cells. A large part of the variation of whole neuron input resistance R_N is due to variation in shape. Membrane resistivity R_m computed from R_N varies accordingly. Statistics of responses to synaptic activation were computed for different dendritic shapes. Magnitude of response variation depended on synapse location, measurement site, and attribute of response.

Keywords: stochastic neurons, dendrites, synapse location, hippocampus, membrane resistivity

1. Introduction

Simulations of biological neural networks require geometry of neurons. Dye filling and tracing of neurons is a time-consuming process, particularly if serial reconstruction is involved. Typically biologically realistic simulations are performed on one or two reconstructed geometries (e.g., Jonas et al., 1993; deSchutter and Bower, 1994a, 1994b). This is an insufficient number of cell shapes when the effects of geometry and sources of variation are considered. Alternatively, arrays of neurons with all the same shape per type of neuron are used in network simulations (e.g., Traub and Miles, 1991; Wilson and Bower, 1989; Manor et al., 1997). To address this undersampling problem, a population of cell shapes is required for a particular type of neuron. If these shapes are sufficiently realistic—that is, if the population of generated cell shapes (statistically) looks and behaves like a population of neuron shapes—then this provides a method for addressing two types of problems. First, this approach can be used to analyze sources of variation of parameter measurements and signal responses due to natural variation of neuron shape. Second, to analyze interaction of functional groups of neurons in a biological neural network, one could generate shapes per type of neuron and distributions of synaptic connections. This would incorporate stochastic variability of neuronal shapes and connections with existing methods of single neuron computations to model interaction of many neurons. In both types of problems, analysis of variation in response due to variation in neuron shape is addressed.

We have developed an algorithm for generating a population of stochastic neurons from a data set of

neurons, whose distributions of morphological features have been measured or can be approximated. A problem of the first type is then addressed using the technique of stochastic neurons. The extensive and detailed analysis of signals in single neurons provides a comparison and is augmented by this strategy.

We used this approach to analyze responses of hippocampal dentate gyrus (DG) granule neurons to stimulation of different parts of the perforant pathways. In the hippocampus, the extrinsic afferents to the dentate gyrus have entorhinal, hippocampal, hypothalamic, septal, and brainstem origins (Cowan et al., 1980; Witter, 1993). Of these, the most important pathway, quantitatively and perhaps functionally, is formed by the axons that arise from the medial and lateral parts of the entorhinal cortex. These projections constitute the perforant pathway, which is divided into the lateral and medial perforant pathways (LPP and MPP), and form part of the intrinsic circuitry of the entorhinal-hippocampal system. The axons in LPP originate from neurons in the lateral entorhinal cortex and preferentially synapse onto the distal third (with respect to the soma) of dendrites in the molecular layer. In contrast, the MPP projects from the medial entorhinal cortex and preferentially synapses onto the middle third of the dendrites. Electrophysiological responses of granule neurons to the activation of the two pathways have been described extensively (Wang et al., 1996; Wang and Wojtowicz, 1997).

We computed the voltage signals within the soma and dendritic tree of the stochastically generated DG neurons, after discretizing the dendritic trees into electrical compartments at high resolution to preserve geometry (Rall, 1959; Hines, 1989; Winslow, 1990). While it is now technically possible to experimentally record these signals (Stuart and Sakmann, 1994), this has been done only in neurons that are easier to access and record than the DG neurons. The simulation results presented here provide results that are currently not (easily) attainable in a biological preparation.

We compared properties of soma excitatory postsynaptic potentials (EPSPs) from the experiments with simulations on different neuronal shapes in the stochastically generated population and with predictions from cable theory of dendrites (Rall, 1964; Rall et al., 1992; Holmes, 1989). Although voltage activated channels have been reported and theoretically analyzed (Stuart and Sakmann, 1994; Cook and Johnston, 1997), we first resolved signals in stochastic neurons with passive membrane. We also commented on values of R_m computed from whole neuron resistance R_N in terms of variation in geometry of neurons. We found that some parameters depend strongly on the shape of dendritic trees while others do not. Preliminary electrophysiological data determined that some aspects of the computed synaptic responses varied in accordance with experimental data obtained by stimulation of LPP and MPP in the hippocampal slice preparation.

Initial results of this work have been published in abstract form (Jou et al., 1995).

2. Methods

2.1. Stochastic Generation of Cell Shapes

A typical dendritic tree traced from a Lucifer Yellow-filled granule neuron in a hippocampal slice preparation is shown in Fig. 1 (see Section 2.4 for details). The algorithm for stochastic generation of cell shapes uses the probability distributions of various shape characteristics observed in granule cells. For example, the soma is approximated by a prolate ellipsoid with length of 18.6 ± 3.43 μm (mean $\pm$ standard deviation) and a width of 10.3 ± 2.06 μm (Claiborne et al., 1990). Assuming that the soma length and width are each normally distributed (for lack of further data), then a new soma can be generated by simply choosing a random number from a normal distribution of mean 18.6 and

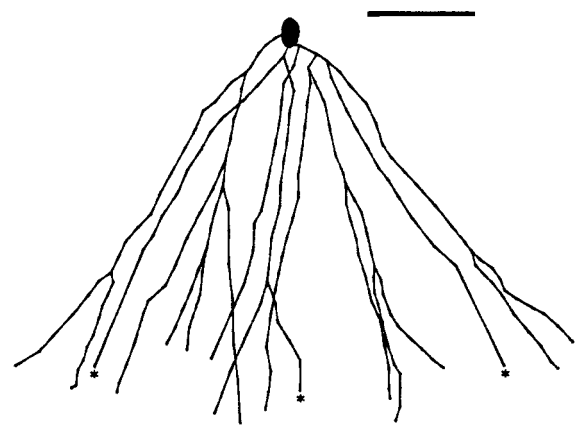

Figure 1. Representative reconstructed image of a Lucifer Yellow–filled DG granule cell (DG) neuron from a hippocampal slice preparation. This cell has been used for quantitation of the dendritic tree (traced shape included in Table 4). Asterisks indicate branches that did not appear to be completly filled with the dye and were arbitrarily extended toward the fissure of the molecular layer. Scale bar: 100 μm.

Table 1. Probability distributions used to generate DG granule cells are the specific distributions used in the implementation of the shape-generation algorithm. In the branch point distribution, $f_B(\omega)$, ω is the normalized distance of a branch point from the soma, where $\omega = 0$ is at the some and $\omega = 1$ is at the distal tips of the dendritic tree (at the fissure). Equation (1) in the text gives the values for $f_B(\omega)$. The noise distribution is a function applied to the x and y coordinates of points along the dendrite to approximate dendritic wiggle, the small turns and deviations which a dendrite exhibits (see text). Starred distributions (*) are based on data from Claiborne et al. (1990), where the standard deviations were computed from the standard error values given in the reference. Note that all dendrites were assumed to terminate at 300 μm.

Item	Distribution	mean $\pm$ sd
Soma length*	Normal	18.6 ± 3.43 μm
Soma width*	Normal	10.3 ± 2.06 μm
Number of primary dendrites*	Normal	1.9 ± 1.37
Number of branch points*	Normal	13 ± 2.97
Branch point location*	Staircase	$f_B(\omega)$
Tree height	Constant	300 μm
Transverse spread*	Normal	325 ± 75.4 μm
Longitudinal spread*	Normal	176 ± 41.1 μm
Noise distribution	Normal	0 ± 1 μm

standard deviation 3.43 for its length in μm, and a second random number from a normal distribution of mean 10.3 and standard deviation 2.06 for its width in μm. A random variate from a normal distribution can be generated using the standard Box-Muller algorithm (Press et al., 1992, sec. 7.2). A population of soma shapes generated in this manner should have the same distribution of lengths and widths as actual soma shapes. This same principle of using probability distributions based on biological observations from real rat granule cell dendritic trees can generate a dendritic tree. The distributions that we used are given in Table 1.

2.2. The Algorithm

A dendritic tree is comprised of connected branch segments, situated between branch points and end points in three dimensions. Generating the dendritic tree involves six steps: (1) generating the branch point normalized distances, (2) connecting the branch points to form a one-dimensional projected tree, (3) mapping the one-dimensional projected tree to a three-dimensional tree, (4) scaling the normalized coordinates to real coordinates, (5) adding dendritic diameters, and (6) adding dendritic wiggle (see Fig. 2).

2.2.1. Generating the Branch Point Locations. The branch points $\{b_1, b_2, \ldots, b_{n_B}\}$ are first generated in normalized coordinates $b_i = (\chi_i, \psi_i, \omega_i)$ and then scaled to actual coordinates (x_i, y_i, z_i). A branch point location distribution $f_B(\omega)$ describes the probability of a branch point occurring at normalized distance ω within the stratum moleculare, where $\omega = 0$ is at the soma in stratum granulosum and $\omega = 1$ is at the hippocampal fissure where the granule cell dendrites terminate (Claiborne et al., 1990). This distribution follows directly from experimental observations of branch points. For example, the branch point probability distribution of Table 1 is

$$f_B(\omega) = \begin{cases} 0.63, & 0 \le \omega \le 1/3, \\ 0.27, & 1/3 < \omega \le 2/3, \\ 0.10, & 2/3 < \omega \le 1, \end{cases} \tag{1}$$

which means that 63% of the branch points occur (uniformly distributed) within the proximal third of the stratum moleculare or dendritic tree, 27% uniformly within the middle third, and 10% uniformly within the distal third.

First, choose the number of branch points n_B following the experimentally observed distribution in Table 1. In general, the probability distribution of branch point normalized distances can take on almost any form. Second, the branch point normalized distances ω_i are generated for any arbitrary probability distribution $f_B(\omega)$ as follows. Choose random variates $u_1, u_2, \ldots, u_{n_B}$ from a uniform random distribution on [0, 1] generated using the Park-Miller algorithm (Press et al., 1992, sec. 7.1). Then apply

$$\omega_i = F_B^{-1}(u_i); \quad i = 1, \ldots, n_B, \tag{2}$$

where $F_B(\omega)$ is the cumulative density function corresponding to $f_B(\omega)$.

$$\begin{aligned} \textit{Probability}\,[\omega_i \le \omega] = F_B(\omega) &= \int_{-\infty}^{\omega} f_B(t)\,dt \\ &= \int_0^{\omega} f_B(t)\,dt, \end{aligned} \tag{3}$$

where $0 \le \omega \le 1$ and $F_B^{-1}(\omega)$ is its inverse. It can be shown by graphical plots of $f_B(\omega)$ versus ω and $F_B(\omega)$ versus ω that the frequency distribution of the set of ω_i points resulting from Eq. (2) is $f_B(\omega)$. Thus, the values of the normalized distances from the soma of the generated branch points will behave like the experimental observations.

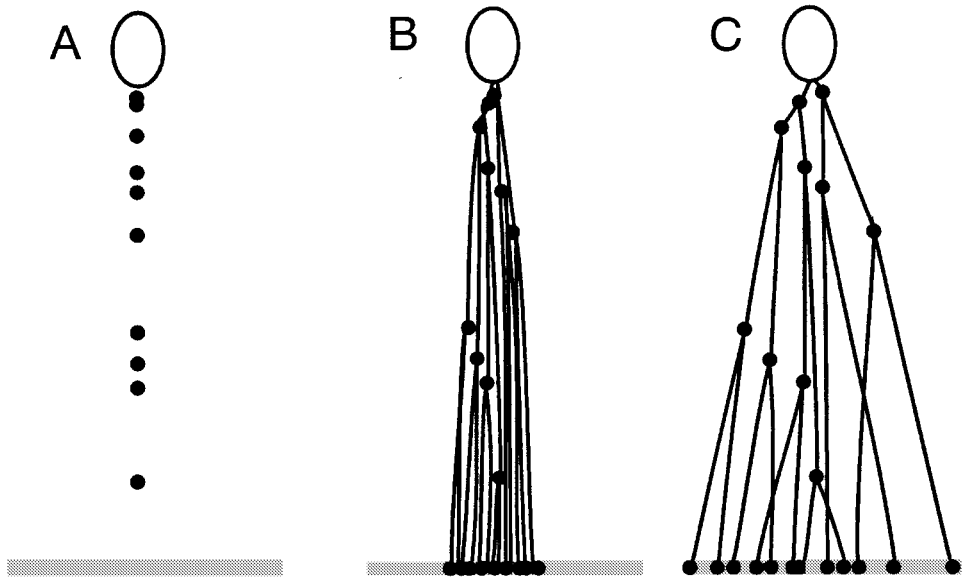

Figure 2. Steps in the algorithm to generate a normalized dendritic tree. Details in text. A: The generated branch points $b_i = (0, 0, \omega_i)$; $i = 1, \ldots, n_B$, where the ω_i are values of normalized distances from the soma shown on the vertical axis ($\omega = 0$ at soma and $\omega = 1$ at bottom). B: Connected branch points to form a 1D collapsed tree. The connections have been expanded slightly so that they are visible; in actuality, all the branch points are still collinear on a single axis underneath the soma, as in the previous step. C: Expanded 1D tree to form a 3D tree, where the branch points are $b_i = (\chi_i, \psi_i, \omega_i)$.

Preliminary to connecting the branch points, sort the ω_i-values so that $\omega_1 \leq \omega_2 \leq \cdots \leq \omega_{n_B}$. Let the branch points be $b_i = (0, 0, \omega_i)$ for $i = 1, \ldots, n_B$ (Fig. 2A).

2.2.2. Connecting the Branch Points to Form a 1D Projected Tree. A branch point by definition represents a point in space where a single *parent dendrite branches into two child dendrites*. The point at the distal tip is called an *end point*. If one assumes that the dendritic tree always extends *outward* from $\omega = 0$ to $\omega = 1$, then it is possible to connect the branch points and end points together in an unambiguous manner to produce a connected tree. At this stage, the branch points are projections on the normalized z-axis (ω-axis).[1]

The branches are connected as follows. Choose the number of primary branches n_P, again drawing from an experimentally derived distribution (Table 1). Create n_P parent segments (primary segments), connecting the soma to branch points $b_1, \ldots, b_{n_P}$. Then for each b_i, create two child segments between b_i and the next two distal points b_j and b_{j+1}, where $i < j$, which do not already have parent dendrites. If no such branch point exists, then create an end point at $\omega = 1$ and connect a child segment to it.

The resulting set of dendritic segments produces a connected tree with the desired characteristics. Since $\omega_i \leq \omega_j$ for $i < j$ and all distal branch end points are located at normalized distance 1, connections are always made for increasing ω, and all the segments will extend in a proximal-to-distal direction. Since connections are always made to the next two distal (most proximal unconnected) points, it is guaranteed that each connected branch point always has one parent and two child dendritic segments. Finally, since this process is done for all branch points in the set B, no branch point is left unconnected (Fig. 2B).

2.2.3. Mapping the 1D Projected Tree to a 3D Tree. This step may be thought of as expanding the generated (projected on ω-axis) tree into a 3D tree by assigning normalized χ and ψ coordinates to each branch point.

First assign (χ, ψ) coordinates to the end points such that they project inside a circle of radius 1. Four end points are assigned values of $(-1, 0)$, $(1, 0)$, $(0, -1)$, and $(0, 1)$. The remaining end points are distributed randomly within the unit circle by generating pairs of uniform random numbers χ, ψ within $[-1, 1]$ and accepting the pair only if $\chi^2 + \psi^2 \leq 1$.

For each of the remaining points, which are all branch points, their (χ, ψ) values are assigned the average values of the distal end points of the two child branches to which it is connected. That is, if the two distalward segments of b_i connect to (χ_1, ψ_1) and (χ_2, ψ_2), then (χ_i, ψ_i) of b_i is set to $((\chi_1 + \chi_2)/2, (\psi_1 + \psi_2)/2)$.

2.2.4. Scaling the Normalized Coordinates to Actual Coordinates. An actual distance H is chosen for the dendritic tree from the height distribution (Table 1), which in this case is constant. Then setting $z_i = H\omega_i$ for $i = 1, \ldots, n_B$ scales the normalized distances to actual distances from the soma.

Longitudinal and transverse spreads l_{tree} and t_{tree} are chosen for the tree from the experimental distribution (Table 1). Scale the unit circle that contains the end points onto an ellipse with diameters l_{tree} and t_{tree} by setting $x = \frac{1}{2} l_{\text{tree}} \chi$ and $y = \frac{1}{2} t_{\text{tree}} \psi$. This produces a spatial arrangement of the dendritic tips consistent with the experimental observation that the widest spread t_{tree} of the tips occurs in the transverse plane of the hippocampus and perpendicular spread l_{tree} in the longitudinal plane (Claiborne et al., 1990). Thus, the set of points $\{b_i; i = 1, \ldots, n_B\}$, where

$$b_i = (x_i, y_i, z_i) = \left(\frac{1}{2} l_{\text{tree}}\, \chi_i, \frac{1}{2} t_{\text{tree}}\, \psi_i, H\omega_i \right),$$

are the actual 3D coordinates of a full dendritic tree (Fig. 2C).

2.2.5. Adding Dendritic Diameters. Each dendritic segment length was divided by the smallest integer such that the size of a compartment is ≤ 1 μm, and each compartment assigned a diameter based on the distance of the compartment's midpoint and using the dendritic diameter versus distance function $K_{\text{diam}}\, d(z)$ obtained from the electron micrograph measurements described below. The length of each compartment is well within 10% of the space constant for a granule neuron, so that numerical accuracy of the compartmental simulations can be assured. Since dendritic diameter is taken to only be a function of distance on the z-axis (not radial from soma or arc length on branch), two child branches at a branch point have the same initial diameter but can taper at different rates, depending on the angle of branching, with respect to the z-axis, or the derivative $\partial d/\partial z$ as function of z. Since we do not have sufficient data to take into account a correlation between soma size and initial dendritic diameter, the same diameter function is used regardless of soma size. Table 2 gives a small sample of dendritic diameters from one rat dentate gyrus that we measured (Section 2.5) and is in agreement with Desmond and Levy (1984). The variations of diameters are presumably due to variations among neurons. We do not have any direct data on this but incorporated this variability in the shrinkage factor, K_{diam} (see Section 2.6).

Table 2. Measurements from two methods used to determine dendritic diameter ± standard deviation (D ± sd) as a function of distance (z) from the soma of DG granule neurons. The number of measurements in n. Not adjusted for shrinkage. See text.

z (μm)	$D \pm$ sd (μm)	n
Method 1		
0–30	2.1 ± 0.63	10
30–60	1.6 ± 0.57	8
60–90	1.1 ± 0.40	7
90–120	1.1 ± 0.63	10
120–150	0.98 ± 0.26	7
150–180	0.94 ± 0.22	5
180–210	0.85 ± 0.49	6
210–240	0.95 ± 0.10	4
240–270	0.81	1
270–300	0.87	2
Method 2		
0–40	1.2 ± 0.38	23
40–80	1.1 ± 0.23	23
80–120	1.1 ± 0.32	27
120–160	0.88 ± 0.26	19
160–200	0.89 ± 0.16	24
200–240	0.79 ± 0.16	25
240–280	0.68 ± 0.24	17
280–320	0.71 ± 0.24	17

2.2.6. Adding Dendritic Wiggle. Finally, the segments of a dendritic tree do not travel in straight lines through the stratum moleculare; rather, they tend to experience small turns or dendritic wiggle. This can be emulated by applying a noise function to the coordinates of each compartment in the XY plane, so that each (x, y) value is given a random normally distributed offset value. This has the effect of slightly increasing the dendritic length of the generated tree. The noise function has a mean of zero to avoid a biased shift in the new positions of the dendritic compartments.

2.3. Implementation of Algorithm

A program that implements this algorithm and uses the distribution functions listed in Table 1 was written using ANSI C. To ensure uniformity across different versions of C, uniform and normal random number generation routines were also written. Uniformly distributed random numbers were generated using the Park-Miller algorithm with a Bays-Durham shuffle, and normally distributed numbers were generated using the Box-Muller method (Press et al., 1992). Each generated shape is assigned an integer number, which also serves as the seed for the random number stream. This gives each shape a unique identifying number and provides a convenient way to reproduce uniquely an entire generated shape from a single number. The program takes a shape number and a value for K_{diam} and produces the corresponding generated shape. A montage of representative generated shapes is shown in Fig. 3. The program, as implemented, can generate a single novel complete granule cell shape in $\leq$10 s on a Sun 3 workstation.

2.4. Digitization of Filled DG Granule Neurons

A DG granule neuron was filled with Lucifer Yellow and photographed onto a slide and traced (Fig. 1). The photographic negative was video digitized using an instrumentation video camera (NC-70, Dage-MTI, Inc., Michigan City, IN 46360) and a Win-TV board (Hauppauge Computer Works, Inc., Hauppauge, NY 11788) on a PC with a program running under DOS (Winslow, 1994). The digitized images were transferred to a Silicon Graphics Indigo computer (Silicon Graphics, Inc., Mountain View, CA 94039-7311), where the scale bar and the nodes and branches of the tree were traced using a tree tracing program (Winslow, 1995). Details on the hardware, data structures, and algorithms used have been described previously (Winslow et al., 1987).

Similar to the representative traced granule neuron shown in Fig. 1, the extent of the dendrites gave a good indication of the location of the hippocampal fissure when the original stained cell is viewed in the slice preparation. The dendrites appeared to terminate almost completely at the fissure, consistent with observations by others (Claiborne et al., 1990). Three dendrites seemed to disappear before reaching the fissure, but they also gradually faded out from the image, likely as a result of projecting above or below the

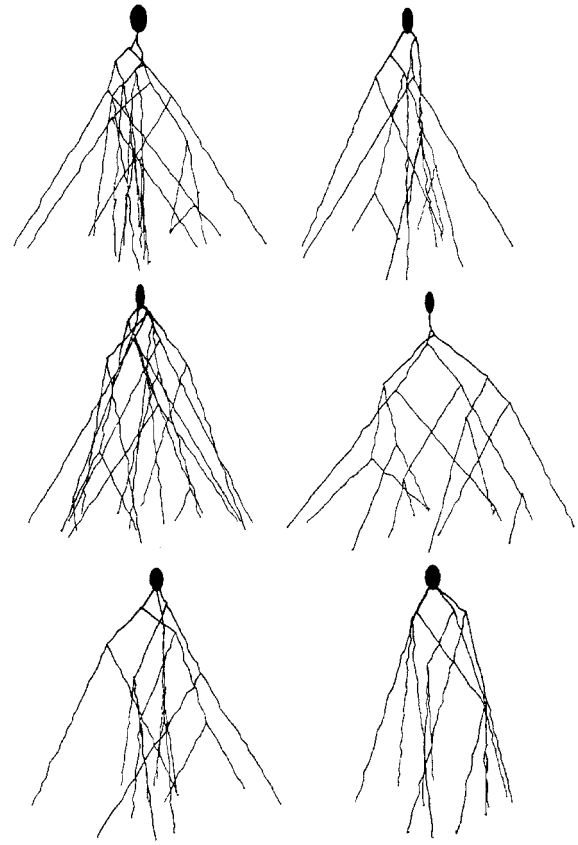

Figure 3. Six representative generated shapes. Shapes such as these were computer-generated using the stochastic algorithm described in the main text. A shape can be uniquely identified and reproduced from a single ID number, which serves as the random number stream seed. Images were generated from the output geometry files using a ray tracer. Clockwise from the upper left: shape 30, 7, 2, 22, 1, and 6.

focal plane. Given that nearly all granule neuron dendrites terminate at the fissure or the pial layer, when the neuron was traced, those dendrites that faded out prematurely were extended by eye in the construction of the traced shape model. A total of three dendritic segments were extended, adding only 247 μm of dendritic length to the tree, for a total dendritic length of 3380 μm. The traced shape had 30 dendritic segments, three primary branches, and a longitudinal spread of 404 μm. These values agreed well with published values on reconstructed granule cells (Table 4). In particular, the dendritic length of this granule cell from a immature (21-day-old) rat agreed well and was even slightly higher than the average dendritic length of an adult rat granule cell. This is consistent with the observation that at three weeks after birth the dendritic arborization

of granule neurons is the same as in adult cells (Cowan et al., 1980), although spine development is not yet fully mature (Cotman et al., 1973; Crain et al., 1973). Therefore, a branch point distribution based on granule neuron dendritic trees in adults can still be used to generate trees in younger, 15- to 30-day-old rats, although adult measurements of spine sizes and densities cannot be used without appropriate scaling.

2.5. *Measurement of Dendritic Diameters*

To complete the statistics for dendrites, diameters are required. Transverse hippocampal slices from a 35-day-old rat were prepared with standard methods for electrophysiological experimentation (Wang et al., 1996). For electron microscopy examination, 400 μm slices were fixed in 6.2% glutaraldehyde in 0.1 M sodium cacodylate buffer (pH 7.4) containing 0.011% $CaCl_2$ and 4% sucrose. After rinsing in buffer, the tissue was postfixed in 2% osmium tetroxide, dehydrated in ethanol, embedded in epoxy, and sectioned on a Reichert "Ultracut" microtome.

Since the long axis of the dendritic tree is approximately perpendicular to incoming axons of the perforant pathway, thin sections (75 nm) were cut in a plane parallel to the dendritic tree and the incoming perforant pathway, so as to facilitate recognition and measurement of the dendritic profiles. Dendritic branches were distinguishable from axons and other cells in the neuropil since they appeared mainly in longitudinal or oblique view, lacked synaptic vesicles, and were generally more electronlucent. Four consecutive sections were micrographed using a Hitachi H-7000 transmission electron microscope.

- *Method 1* In five separate fields, diameter measurements were made of dendritic profiles that extended longitudinally or obliquely. Each field, which extended from the cell body layer to the fissure of the molecular layer, was about 360 by 30 μm. Measurements of 10 to 20 profiles from each field were made by a naive observer. In cases where the diameter of the dendrite was not uniform along its length, it was assumed that the dendrite had been cut obliquely to its long axis, so the smallest ellipsoid diameter (true diameter) was measured.
- *Method 2* The dendritic diameter measurements were independently confirmed in another field from a different area of the same dentate gyrus by a different observer. A square grid (20×20 μm per square) was overlaid on each micrograph. Coordinates corresponding to the squares were uniformly, randomly chosen with a density of approximately 24 samples per micrograph (total area 43,000 μm^2). Within each randomly chosen square, a measurement of dendritic diameter was made if a dendrite could be identified within the chosen sample. Dendrites were identified by (1) electronlucent, (2) presence of postsynaptic density, (3) presence of mictrotubles, and (4) lack of vesicles. The number of these identified features (one to four) per observed dendrite and diameter were recorded. These values were used to compute a weighted mean of diameters, so that diameters that came from unequivocal dendrites contributed more to the mean than tenuously identified dendrites.

The results from these two methods were found not to differ significantly and are reported in Table 2. They are similar to those of Desmond and Levy (1984) obtained from adult animals. Using a generalized least-squares curve-fitting procedure, diameter as a function of distance, z, from the soma within the dendritic layer was best fit by

$$f_d(z) = 1.713 \exp(-z/47.70) + 0.8626, \quad (4)$$

where f_d and z are in μm.

We corrected for tissue shrinkage, which occurred as a result of the chemical processing for electron microscopy (Hayat, 1981), by using a unitless scaling factor, $K_{\text{diam}} = D_t / D_m$, where D_t = true diameter, D_m = measured diameter, and S = shrinkage = $(D_t - D_m)/D_t$. In the computation of passive parameters and the simulations, K_{diam} was varied from between 1.0 ($S = 0$) to 1.4 ($S = 29\%$). The function

$$d(z) = K_{\text{diam}} f_d(z) \quad (5)$$

is used in both the generated shapes and the traced shape to set the dendritic diameters. Shrinkage of 30 to 40%, including extracellular space, is expected from the EM tissue preparation procedure (Hayat, 1981). However, the exact shrinkage of the dendrites is not known and dendrites have lipid membranes, small cross-sections, and intracellular organelles, thus they presumably shrink less. Consequently, we chose $K_{\text{diam}} = 1.2$ (S =17%).

2.6. *Dendritic Spines*

Up to 50% of the dendritic surface membrane may be attributed to the presence of dendritic spines (Hama

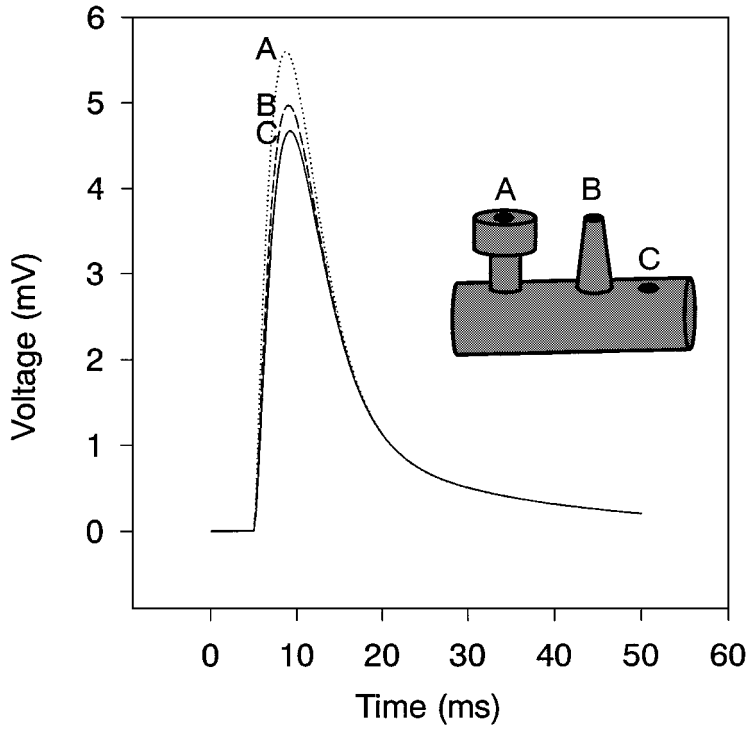

Figure 4. Local voltage responses to synaptic conductance placed on the different types of spines. The spine was located on the medial region of the dendritic tree at 200 μm from the soma in generated cell shape #49. A: An expanded spine, SPE. B: A simple spine, SP. C: No spine with dendritic shaft only for comparison.

et al., 1989), which are small, fingerlike protrusions extending from the dendrites of many neurons and often, but not always, terminating in bulbous expansions (Fig. 4). They increase the effective surface area, thereby increasing the electrotonic length of dendritic segments and electrotonically distancing the synapse from the soma (Holmes, 1989; Stratford et al., 1989; Holmes and Levy, 1990; Holmes and Rall, 1992; Segev et al., 1992; and discussion in Rall et al., 1992). Given the large number of spines on a single granule neuron, explicit creation of one or two compartments per spine on the dendritic tree generates a large number of compartments requiring more equations and time-consuming simulations. Using the technique of Major (1992), we represented the spines on each dendritic segment by increasing the length and diameter of the segment and replacing the spiny dendrite with a single longer and wider smooth (spineless) dendrite.

The surface area contribution of spines was assumed to be $K_{\text{spine}}A$ μm^2 per 1 μm of dendrite (arc length), where $A = 4.180$, 2.806, 2.401 μm^2 for the proximal, middle, and distal portions, respectively, of the stratum moleculare (Hama et al., 1989, Table 3). K_{spine} is the scaling parameter that was introduced to address the uncertainty regarding the actual spine density and size on granule neurons of immature rats. Immature spines are not as large or elaborate and do not appear at the same densities as adult spines (unpublished observation). We scaled down the adult spine estimates by K_{spine}, where $K_{\text{spine}} < 1$ is interpreted as modeling smaller, less elaborate, and less densely distributed spines. $K_{\text{spine}} = 0.5$ means the spine surface areas are half that of the adult spine surface areas as measured by Hama et al. (1989). The simulated cells have half the number of spines as an adult rat granule neuron (Desmond and Levy, 1985) or the full adult number of spines, but each spine has half the adult surface area. More likely, there is a combination of both smaller and fewer spines in the simulated immature rat granule neuron compared with an adult.

Our data are based on six dendritic segments (three from lateral and three from medial perforant pathway) with a total length of 10.7 μm. All these segments were fully reconstructed from serial EM sections. We counted 35 synapses contacting the dendrites and only five contacting spines. All spines were very small,

Table 3. Parameters used in the simulations. The spine values are based on adult-sized rat DG granule neurons (Hama et al., 1989). Each linear parameter is scaled by $K_{\text{spine}}^{1/2}$, so that the final surface area of all the spines is scaled by a factor of K_{spine}. See text.

Parameter	Value
α	0.5
Δt	0.25
C_m	0.7 μF/cm^2
$g_{\max}$	0.45 nS
K_{spine}	0.5
K_{diam}	1.2
R_i	150 Ω cm
R_m	78.3 KΩ cm^2
V_{rest}	-69.8 mV
Compartment length	≤ 1 μm
Spine Area	μm^2/μm dendrite length
Proximal third	K_{spine} 4.180
Middle third	K_{spine} 2.806
Distal third	K_{spine} 2.401
SPE Spines	
Head Height	$K_{\text{spine}}^{1/2}$ 0.51 μm
Head diameter	$K_{\text{spine}}^{1/2}$ 0.50 μm
Base height	$K_{\text{spine}}^{1/2}$ 0.752 μm
Base diameter	$K_{\text{spine}}^{1/2}$ 0.185 μm
SP Spines	
Base height	$K_{\text{spine}}^{1/2}$ 1.253 μm
Base diameter	$K_{\text{spine}}^{1/2}$ 0.333 μm
Tip diameter	$K_{\text{spine}}^{1/2}$ 0.258 μm

measuring 0.5 to 1 μm in length and diameter. Two other spinelike projections were devoid of synapses. Seven spines per 10.7 μm of the dendritic length amounts to 0.65 spines/μm, a much smaller spine density than the reported 1.4 spines/μm in adult animals (Desmond and Levy, 1985), consistent with our estimate of $K_{\text{spine}} = 0.5$. To implement this, we wrote a program that takes a dendritic tree shape (such as the traced shape or a generated shape) and for a given value of K_{spine} calculates the spine-collapsed version. For most of the simulations $K_{\text{spine}} = 0.5$ was used.

2.7. *Shape to Compartments*

The 3D description of a dendritic tree has the form of a list of *xyz* coordinates of locations of the soma, branch points, and distal tips. This representation gives the visual lifelike shape and exact shape measurements, which are then the data used for the shape statistics. The dendrite is discretized into compartments, whereby each branch point and dendrite end points are centers of compartments, and each branch is subdivided into compartments. Because the structure is in 3D, the true lengths of branches must be calculated from the 3D distance between branch points.

The discretized neuron, when represented by compartments for simulation, is a list of tuples, one per compartment, consisting of compartment number, compartment location, compartment parameters, list of compartments to which it connected, and input synapse number.

2.8. *Simulation of Synaptic Potentials*

A set of 50 different cell shapes was generated and converted into compartmental models. The compartments assigned in generating the neuron were used for the simulations. Thus, the minimum and maximum compartment lengths are 0.5 and 1.0 μm, respectively. The average number of compartments per simulation was at least 3,430, which corresponds to the total length of the generated dendritic tree. All computer simulations were done using NEURON 2.0 (Hines, 1984, 1989) on either a SUN-3 running BSD Unix or an Intel 486DX33 PC running Linux. Simulation parameters are given in Table 3. When an activated synapse was on a spine, these spines were explicitly modeled, using one or two compartments with the dimensions given in Table 3, with spine measurements from Hama et al. (1989). The remaining spines were implicitly represented in the simulations, using the spine collapse procedure. The time course of synaptic conductance was simulated by the α function, $g_{\max}(\alpha t)\exp(1-\alpha t)$, where $\alpha = 0.5$ and $g_{\max}$ were chosen, so that simulated responses at the soma had shape and amplitude similar to those of recorded responses in granule cells.

2.9. *Electrophysiological Recordings in Hippocampal Slices*

Recordings and analysis of synaptic responses were described in our recent publications (Wang et al., 1996; Wang and Wojtowicz, 1997). All recordings were performed from cell bodies of the granule neurons in the whole-cell configuration. Input resistances were measured by applying 10 mV, 100 ms depolarizing voltage

steps from a resting membrane potential (approximately −70 mV) and measuring steady-state currents. Synaptic responses were evoked at 0.1 Hz by electrical stimulation of afferent axons in the outer (LPP) and middle (MPP) molecular layers. Stimulus current was adjusted to produce approximately equal amplitudes of evoked excitatory potentials (EPSPs) from LPP and MPP, as recorded in the cell body.

3. Results

3.1. Verification of the Algorithm

Verification of the algorithm, and overall correctness of the program that implemented the algorithm, was done by ascertaining the realism and statistics of the generated shapes, of which a representative sample is shown in Fig. 3. Population statistics of tree measurements, some of which were not directly based on distributions used in the algorithm, were computed on 100 generated shapes, shapes 0 to 99. The number of dendritic segments, number of primary branches, transverse spread, longitudinal spread, dendritic length, and tree shape (the ratio of longitudinal spread to transverse spread) were evaluated. These statistics for the generated shapes were then compared with those same statistics published in the literature (Table 4).

The generated cell shapes appear to be realistic. In all cases the mean statistics are comparable, implying that on average the generated shapes are similar to actual cell shapes, at least with respect to the number of dendritic segments, number of primary branches, transverse spread, longitudinal spread, dendritic length, and tree shape. Further, the standard deviations of all the statistics are also comparable. This suggests that the population of generated shapes also encapsulates the same variability expected in a population of real granule cells *in vivo*. Thus, we conclude that our algorithm and program, which implemented the algorithm, are valid for their purpose of generating this type of neuron.

3.2. Passive Parameters

In addition to morphological details, the passive parameters of granule neurons must be determined before simulations can be performed. The whole cell input resistance $R_N = 280.4 \pm 150.2\,\mathrm{M\Omega}$ was measured experimentally in 320 granule neurons. This value is higher than R_N reported for adult rats (Staley et al., 1992) as may be expected if the dendritic tree and soma were more compact in our immature animals.

Given a value of axoplasmic resistivity R_i, the previously obtained measurement of R_N, and a specific cell shape (either the traced cell shape or a generated shape), a unique value for membrane resistivity R_m may be computed using a recursive procedure. Instead of using R_i, R_m and a given shape to compute R_N (Rall, 1957, 1989; Segev et al., 1989; Nitzan et al., 1990), we computed the theoretical value of R_m such that $R_N = 280.4\,\mathrm{M\Omega}$ for each generated shape (Fig. 5). Because of recent evidence that the internal axoplasmic resistivity R_i is actually much higher than previously thought (Shelton, 1985; Jonas et al., 1993; Rapp et al., 1994; Major et al., 1994; Thurbon et al., 1994; Borst and Haag 1996), computations were performed

Table 4. Tree statistics comparing published values from actual DG granule neurons, computed values from the traced shape, and computed values from 100 generated shapes. Published and generated shape values are ± standard deviation. Tree shape is the ratio of longitudinal spread to transverse spread. Longitudinal spread and tree shape from the traced shape is not available since it was projected on to a single plane. Note that the means of actual versus generated shapes are not significantly different. Published values are from Claiborne et al. (1990).

Characteristic	Published values	Traced shape	Generated shapes
n	48	1	100
Dendritic segments	29 ± 6.86	30	25.8 ± 6.11
Primary branches	1.9 ± 1.39	3	2.41 ± 1.26
Transverse spread (μm)	325 ± 75.41	404	314 ± 66.8
Longitudinal spread (μm)	176 ± 41.13	—	177 ± 39.0
Dendritic length (μm)	3221 ± 535	3380.24	3430 ± 802
Tree shape	0.56 ± 0.21	—	0.54 ± 0.20

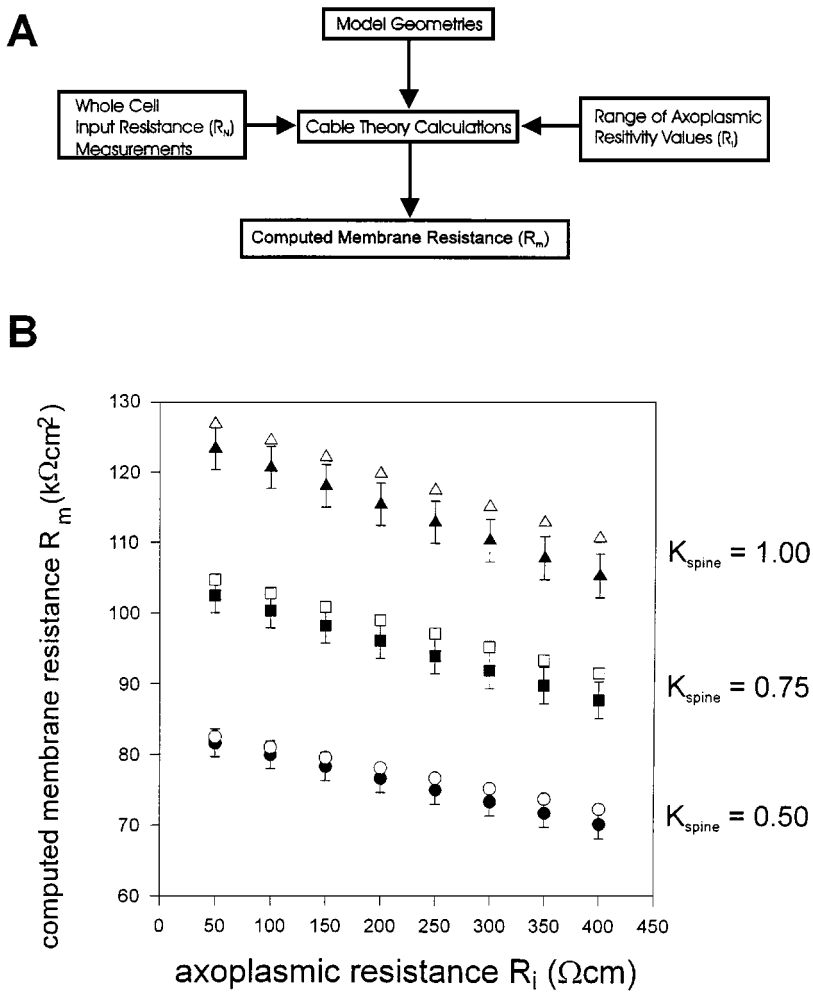

Figure 5. A: Pathway to compute membrane resistivity R_m. Given estimates of passive parameters R_m and R_i, and a cell shape, one can obtain a theoretical R_N from cable theory. In this article, R_N was experimentally measured, and R_i varied across a physiologically plausible range. Model geometries came from a tracing of an actual DG cell as well as from computer-generated shapes. B: Computed membrane resistivity R_m for generated and traced DG cell shapes, corrected for shrinkage. The dendritic diameters used in the shapes have been expanded to account for tissue shrinkage ($K_{\text{diam}} = 1.2$). Points are the R_i and R_m values such that the measured R_N is 280.4 MΩ from young rat DG cells. Hollow shapes are for the traced shape; filled shapes are average values for 100 generated shapes. Triangles (upper curve): $K_{\text{spine}} = 1.0$, which gives spine surface area $K_{\text{spine}}A = 4.180$, 2.806, and 2.401 μm^2 per μm of dendrite for the proximal, middle, and distal thirds of the dendritic tree; squares (middle curve): $K_{\text{spine}} = 0.75$, giving $K_{\text{spine}}A = 3.135$, 2.105, and 1.801 μm^2 per μm; circles (lower curve): $K_{\text{spine}} = 0.50$, giving $K_{\text{spine}}A = 2.090$, 1.403, and 1.201 μm^2 per μm. The values corresponding to $K_{\text{spine}} = 0.50$ are most appropriate for our young preparation. Bars are standard error.

from below the traditional value of $R_i = 70$ Ω cm, to $R_i = 400$ Ω cm, which are generous bounds on the true R_i. Assuming tissue shrinkage factor $K_{\text{diam}} = 1.2$, the results obtained are shown in Fig. 5B.

The nominal value of C_m used in the simulations was 0.7 μ F/cm^2, which is lower than the usual value of 1.0 μ F/cm^2 but is currently believed to be the most accurate value of membrane capacitance (Fettiplace et al., 1971; Takashima and Schwan, 1974; Benz et al., 1975; Takashima, 1976; Haydon et al., 1980; Major et al., 1994). However, if C_m is actually higher (e.g., Borst and Haag, 1996), this will significantly alter the simulated responses (see below). The predicted response will be more sluggish, with a slower rise time, lower amplitude, and longer time constant (not shown) and would not agree with our data.

Two agreements with theory may be seen at this point. First, the mean computed R_m of our morphologically realistic granule neurons, which were stochastically generated, is very dependent on the surface area of spines, as previously shown (e.g., Rall et al., 1992; Stratford et al., 1989; Holmes 1989; Holmes and Rall, 1992; Segev et al., 1989). The standard deviations associated with mean R_m computed for different K_{spine} values vary linearly with respect to K_{spine} (3.0, 2.4, 1.8 KΩ cm^2 for $K_{\text{spine}} = 1.00, 0.75, 0.50$, respectively) but is constant with respect to R_i (as shown in Fig. 5). The large differences in computed R_m values due to different choices of K_{spine} mean that an accurate measurement of the spatial extent of spines is critical, if an exact determination of R_m is desired using this method. Second, the computed R_m is slightly decreasing for increasing axoplasmic resistivity R_i varying from 50 to 400 Ω cm, which agrees with Rall's equation (Rall, 1989, Eq. (2.46)) $R_N^{-1} = A_D \tanh(L)/R_m L$. This relates R_N to R_m, and R_i for an equivalent cylinder, where area $A_D = \pi l d$ for length l, diameter d, and $L = l/\lambda$. Other versions of this formula can be found in the literature (e.g., Rall et al., 1992; Johnston and Wu, 1995, sec. 4.8). Figure 5, computed for fine spatial discretization resolution per stochastically generated neuron, implies that R_m values typically computed from the membrane time constant τ may be incorrect by at most 10%, despite recent estimates of R_i that may be several times higher than 70 Ω cm (Spruston et al., 1993, 1994).

The computed R_m values suggest that $K_{\text{spine}} = 0.5$ is reasonable. When the higher values of $K_{\text{spine}} = 0.75$ and $K_{\text{spine}} = 1.00$ were used to compute R_m, these R_m values do not agree with other estimates based on the membrane time constant τ measured to be 56.3 ms in a similar experimental preparation (immature rat DG granule cells) (Zhang et al., 1993). Assuming that $\tau = 56.3$ ms and that $C_m = 0.7$ μF/cm^2, then from $\tau = R_m C_m$ one obtains $R_m = 80.4$ KΩ cm^2. This is very close to the theoretical R_m values that we computed when $K_{\text{spine}} = 0.5$ (Table 5).

The variation in R_m of the generated shapes shown in Table 5 is due to variation in shape alone because the computed R_m per shape is the value such that $R_N = 280.4$ MΩ, the mean of the experimentally obtained values. Additionally, the large variation of experimental R_N measurements may be partially due to the different tree geometries. To test this hypothesis, R_m was fixed at 78.3 KΩ cm^2 ($R_i = 150$ Ω cm, $K_{\text{spine}} = 0.5$) and then R_N computed for 100 randomly generated shapes. The result was an R_N of 296.5$\pm$ 83.2 MΩ. Since R_m was constant, the standard deviation of 83.2 MΩ is the result of the shape variation within the population of generated cells.

Table 5. Computed membrane resistivity R_m for generated shapes. All shapes have been spine-collapsed assuming spine surface areas of $A = 4.180, 2.806, 2.401$ μm^2 per μm of dendrite at the proximal, middle and distal portions. The R_m is computed such that, for a given geometry, R_i and K_{spine}, it produces the whole cell input resistance $R_N = 280.4$ MΩ, which is the average of the experimentally obtained values (see text). A tissue shrinkage factor has been assumed ($K_{\text{diam}} = 1.2$). The mean R_m and standard deviation ($n = 100$) are shown. Same values are shown in Fig. 7.

$K_{\text{spine}} =$	0.50	0.75	1.00
R_i (Ω cm)	R_m for generated shapes (KΩ cm^2)		
50	81.6 ± 19.6	102 ± 24.5	123 ± 29.5
100	80.0 ± 19.7	100 ± 24.7	121 ± 29.7
150	78.3 ± 19.8	98.2 ± 24.8	118 ± 29.9
200	76.7 ± 19.8	96.0 ± 25.0	115 ± 30.1
250	75.0 ± 20.1	93.9 ± 25.2	113 ± 30.3
300	73.4 ± 20.3	91.9 ± 25.4	110 ± 30.5
350	71.8 ± 20.4	89.8 ± 25.6	108 ± 30.7
400	70.2 ± 20.6	87.8 ± 25.8	105 ± 31.0

Uniformly changing the surface area contribution of spines can emulate the presence of spines during varying stages of development. When spine sizes were changed along with tree geometries, the resulting standard deviation was similar to that produced by changing tree geometries alone; fixing R_m and R_i as before, but varying K_{spine} uniformly between 0.5 and 0.9 over 300 generated shapes, produced an R_N of 248.2 $\pm$ 77.8 MΩ. Similarly, uniformly varying the membrane resistivity in the range 70.0 to 85.0 KΩ cm^2 produced a similar standard deviation; the computed R_N over 400 generated shapes was 273.2 ± 64.8 MΩ. These observations are consistent with the idea that the cell-to-cell variance associated with experimentally measured R_N values in real cells can be at least partially due to their different tree geometries as suggested by Rall (1959).

3.3. Synaptic Potential Simulations

After activating a synapse, a voltage depolarization occurs on the synapse-bearing spine or shaft then spreads throughout the dendritic tree. What eventually

conducts to the cell body is what is observed in whole-cell current clamp recordings.

As shown in Fig. 4 (inset), dendritic spines may be without an expansion of the spine head (SP), or they may have a terminal expansion of the spine head (SPE). When the synapse occurs on the tip of an SP spine or the head of an SPE spine, the spine response inside the tip or the head is amplified (Fig. 4). This was expected from theoretical considerations; since the spine has a greater input resistance than the parent dendrite, the same synaptic conductance produces more depolarization at the spine than at the dendrite (Koch and Zador, 1993). The simulated depolarization inside the spine head of an SPE spine was approximately 20% greater than the response to the same synapse when placed directly on the shaft. The spine response inside the tip of an SP spine had an amplitude of 4.96 mV, which is also slightly larger (by 6%) than the response to a shaft synapse but not as large as the SPE response. This is likely because the neck diameter of SP spine is larger than that of an SPE spine

Despite the initial differences in the synaptic response, however, by the time the depolarization has conducted to the dendritic shaft that contains the spine, the response to a spine synapse becomes virtually identical with the response to the same synapse placed directly on the shaft. This implies that when studying the conducted soma or shaft response to synaptic activation, the exact synapse configuration is not important. This is consistent with previous calculations that current loss across the spine neck is negligible (Koch and Zador, 1993), since current loss is proportional to membrane surface area and the spine neck area is very small (Harris and Stevens, 1989). Hence, the remaining simulations were performed with the synapse placed directly on the shaft.

3.4. Responses to LPP and MPP Stimulation

Since LPP and MPP make excitatory synaptic connections with the the distal and medial thirds, respectively, of the dendritic tree of granule neurons as shown in Fig. 6, can the responses at the soma due to stimulation of the LPP and MPP be distinguished? We address this question by simulations on the generated set of neurons and compare the results with simulations in which LPP and LPP were individually stimulated for the same recorded cell. The inset in Fig. 6 localizes the measurements of interest on the waveform recorded at the soma for the simulations and the experiments.

3.5. Effect of Dendritic Diameter on Simulated Local and Conducted EPSPs

When the location of the synapse was varied along the dendrite, it was found that the local response varied significantly. In particular, the amplitude of the local shaft depolarization depends greatly on the distance of the synapse from the soma; distal synapses consistently depolarized the local dendritic tree much more greatly than the similar synapse located more medially (Fig. 7). This is primarily because distal dendrites are thinner and tend to be closer to a terminated dendrite, compared with a more proximal dendrite, which is thicker, and the incoming current can spread in two directions. Distal local responses also tended to fall faster. This implies that LPP synapses can cause much larger and shorter lasting depolarizations in the local dendritic tree than MPP synapses. Half width and decay times are shorter in LPP regions (see Table 6) in spite of slightly longer rise times.

These local differences in shapes and amplitudes tended to disappear by the time the responses had conducted to the soma (Fig. 7). With the exception of the rise time of the conducted response, the location of the originating synapse cannot be easily determined from the shape of the conducted response, at least in terms of their amplitudes, half-widths, or decay time. However, more medial synapses had more rapid rise times at the cell body than more distal synapses.

Figure 8 shows the peak amplitude of the transient response along an entire dendritic tree to a LPP and to a MPP synapse. This profile of the transient response in a specific dendritic tree shape is similar to the steady state result of Rall and Rinzel (1973) using equivalent cylinders. There is substantial distal-to-proximal decrement within even the single branch that contains the synapse. By the time the synaptic response has passed its first or second branch point, there is no longer an amplitude difference between the response to an LPP or an MPP synapse. However, there is some difference in the distal direction (compare the distal tips). Because a distal synaptic response appears to decay much more rapidly along the dendritic tree than a proximal synaptic response, the amplitudes of both responses appear very similar by the time they have conducted to the upper half of the dendritic tree (Table 7).

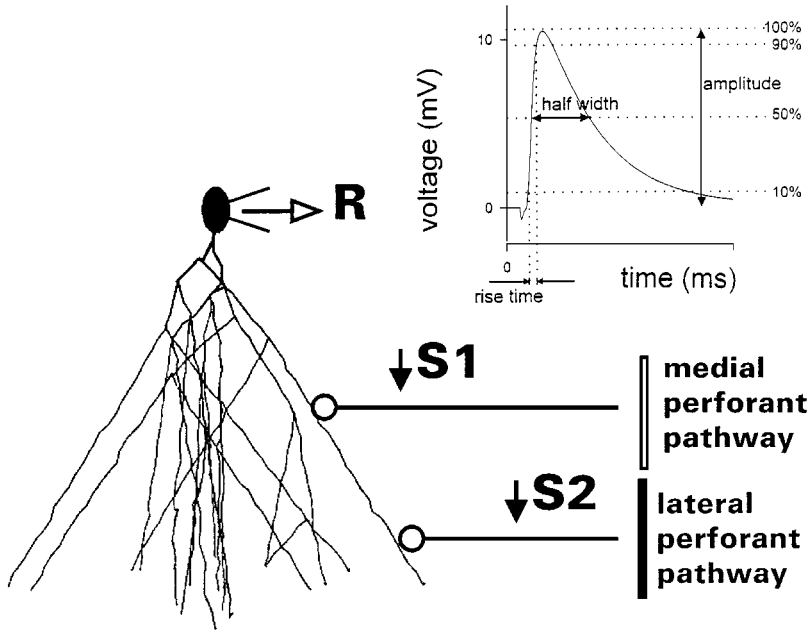

Figure 6. Experimental arrangement for stimulating and recording synaptic responses in lateral and medial perforant afferents in the hippocampal slice preparation from rat. The stimulating electrodes made of fine tungsten wires were placed in middle (S1) and the outer (S2) molecular layer to activate two independent bundles of afferent pathways. This results in activation of synapses located in the middle and distal third of the dendritic tree, respectively of dentate granule cells. The resulting voltage depolarizations were measured at the soma of the dentate granule neuron using the whole-cell recording under current-clamp configuration (R). The granule cell illustrated here is one of the stochastically generated shapes described in this article. Inset: The waveform characteristics amplitude, 10 to 90% rise time, and half width of an evoked response at the soma due to stimulation of the medial perforant pathway (S1) or the lateral perforant pathway (S2). These characteristics, along with the decay time (t_{dt}, not shown here), are used to measure the shapes of synaptic responses. The amplitude is the voltage difference between the peak of the response and the baseline. The 10 to 90% rise time is the time it takes for the rising phase to go from 10 to 90% of the peak voltage attained. The half width is the time the response requires to go from 50% of the peak voltage in the rising phase to 50% of the peak voltage in the falling phase. The decay time is the value t_{dt}, which best fits the curve $\exp(-t/t_{dt})$ to the falling phase of the response.

3.6. Comparison of Response Differences Due to Shape

To directly analyze response differences due to variation in shape and location of synaptic input, we compared simulated responses from different stochastically generated neurons by plotting measurements of the response versus distance from soma. Figure 9 shows the rise times (10 to 90%) and peak amplitudes of local and conducted responses. Fifty different generated cell and dendritic tree shapes were used, with a total of 1,318 synapse locations (an average of 26 different random locations within the dendritic arbour of a given cell shape). All parameters, except for synapse locations, were unchanged; thus, the scattering observed in the figures is indicative of the variation due purely to geometric differences. Of the 1,318 synapse locations, 396 were classified as MPP (had a distance between 100 and 200 μm), and 438 were classified as LPP (had a distance between 200 and 300 μm). Table 6 gives an overall picture from comparing inputs from LPP and MPP synapses. The scatter of the simulated data due to morphology is presented in Fig. 9. For a given distance from the soma (horizontal axis), each data point is the simulated response from a different stochastically generated neuron. That is, the distribution shows the effect of variation in shape alone.

3.7. Comparison of Responses from Stimulation of Lateral and Medial Pathways

In the experiments, examination of the averaged responses from 12 neurons showed a significant difference ($P < 0.05$, t-test) in the 10 to 90% rise times between the two pathways whereas the amplitudes, the half-widths, and the decay times t_{dt} did not differ significantly Fig. 10).

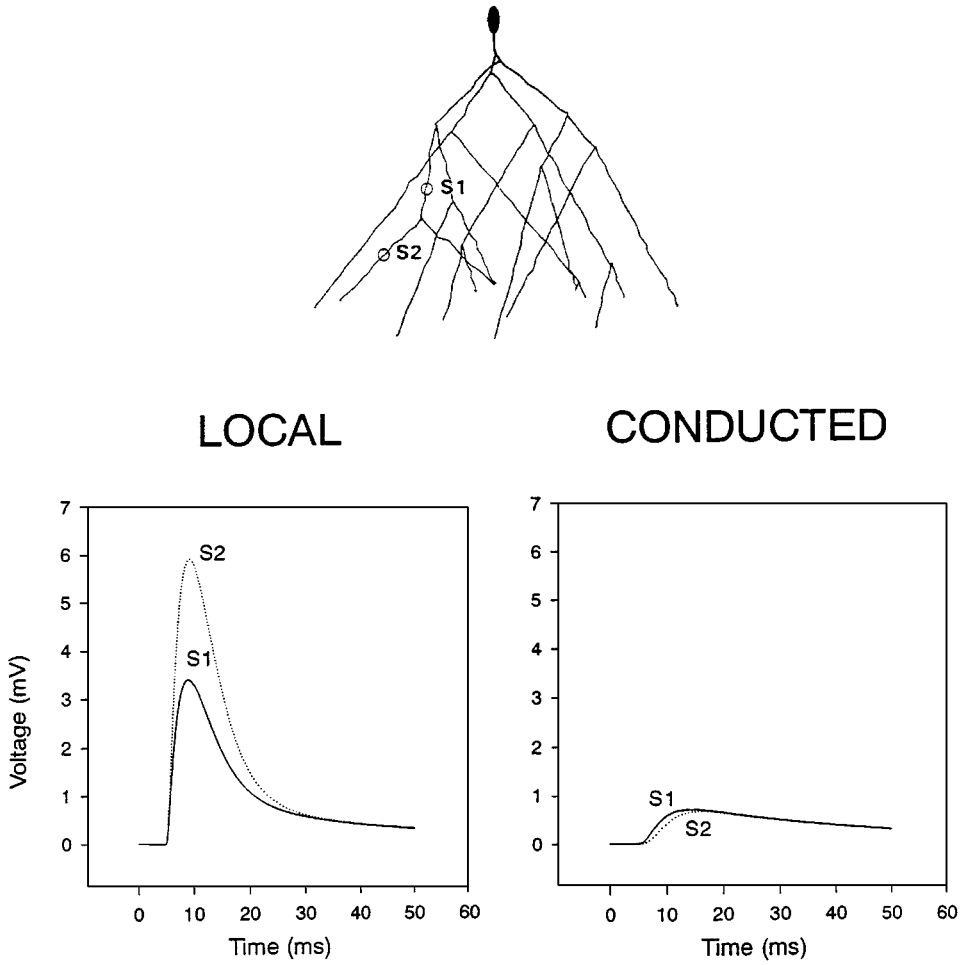

Figure 7. Examples of local and conducted voltage responses to synaptic activation in distal (S2) and medial (S1) dendrites of generated shape #22. The local responses in the dendrite differed dramatically in amplitudes, whereas the conducted responses in the soma differed in rise times.

Overall, the soma EPSP shape parameters suggest that the averaged synaptic responses originating in the middle third of the dendritic tree (via the MPP) can be distinguished from the ones originating in the distal third (via the LPP) on the basis of their rise times.

4. Discussion

4.1. Stochastically Generated Neurons

The use of stochastically generated neurons is a practical way of analyzing influences of shape on parameter and response measurements. We have demonstrated a method of generating a distribution of neuron shapes based on statistics of morphology and applied this method in an investigation of variation of synaptic responses and membrane resistance estimates due to neuron shape. We have used only passive membrane to keep separate the effects of shape from effects of active membrane (e.g., Cook and Johnston, 1997).

4.2. Variation of Parameters

Simulations of synaptic potentials at different dendritic locations on the population of dendritic shapes reveal striking, previously unreported variations among the synaptic parameters. For example, the rise times and the amplitudes of the synaptic potentials depended strongly on the dendritic location with respect to the cell soma (Fig. 9A, B; Table 6). The rise times were similar for different shapes and dendritic locations when recorded locally but showed a clear decline for

Table 6. Summary of comparison of simulated responses from different stochastically generated neurons, shown as local and conducted response measurements versus the two regions of input. Same data as shown in Fig. 11 but only those results corresponding to MPP and LPP regions, respectively located at 100–200 and 200–300 μm from the soma. The measurements of response are defined as in Fig. 2. Values are mean $\pm$ standard deviation.

Characteristic	MPP responses	LPP responses
Local responses		
n	396	438
Amplitude (mV)	3.45 ± 0.832	5.08 ± 0.589
10–90% rise time (ms)	2.21 ± 0.152	2.28 ± 0.072
Half width (ms)	12.5 ± 5.27	8.28 ± 1.40
Decay time, t_{dt} (ms)	18.1 ± 5.25	13.1 ± 1.82
Conducted responses		
n	396	438
Amplitude (mV)	0.597 ± 0.139	0.586 ± 0.152
10–90% rise time (ms)	4.73 ± 0.452	5.40 ± 0.364
Half width (ms)	29.7 ± 4.21	30.3 ± 4.56
Decay time, t_{dt} (ms)	36.1 ± 6.40	36.6 ± 6.51

Table 7. Effect of shrinkage of dendritic diameter on simulated local and conducted responses. The response on the synapse-containing dendrite shaft (local response) and at the soma (conducted response) varies with the diameter of the dendrites in the tree. To test this, the raw diameter curve observed from EM photos was multiplied by $K_{\text{diam}} = 1.0$ (assumed no shrinkage occurred during the EM preparation), $K_{\text{diam}} = 1.2$ (17% shrinkage), and $K_{\text{diam}} = 1.4$ (29% shrinkage). The shapes of these responses are described here in terms of their amplitudes, 10 to 90% rise times, half-widths, and decay time (t_{dt}). The responses shown are for a synapse located in the MPP region. $K_{\text{diam}} = 1.2$ is the nominal value used in the main simulations.

Diameter K_{diam}	Amplitude (mV)	Rise time (ms)	Half width (ms)	t_{dt} (ms)
Local response				
1.0	5.67	2.50	9.30	9.72
1.2	4.67	2.34	8.59	9.45
1.4	3.90	2.23	8.19	9.42
Conducted response				
1.0	0.600	6.20	28.3	32.3
1.2	0.660	5.84	26.6	30.1
1.4	0.686	5.60	25.8	29.1

proximal dendritic locations when recorded at the soma (Fig. 9B). The amplitudes varied locally within the dendrites but decayed at the soma to values that were essentially similar for different shapes and dendritic locations (Fig. 9A, bottom panels). In contrast, the half-widths and decay times varied strongly with dendritic shapes, especially when conducted toward the soma (right-hand panels in Fig. 9B). The local, but not the conducted, responses also depended strongly on the dendritic locations. These simulations have clear

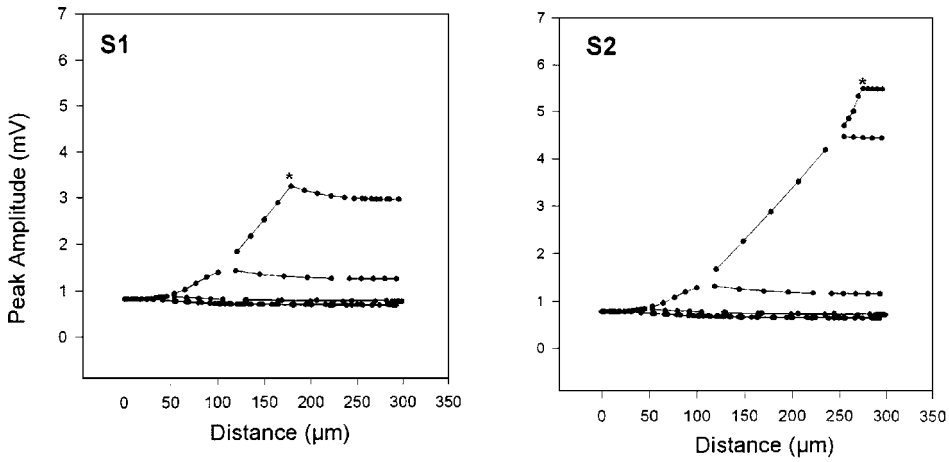

Figure 8. The same synaptic locations on the same neuron as in Fig. 7 show the characteristic decay profiles of the dendritic voltages generated at two locations. A synapse located in the middle dendrite (S1) produced peak voltage of approximately 3.2 mV near the synapse (*), which rapidly decayed to about 1.7 mV at the first branch and to 0.8 mV at the soma. The potentials invading the adjacent branches through the branch points (breaks in the curves) are also plotted. Synapses located in the distal dendrite (S2) produced peak voltage of approximately 5.5. mV (*), which decayed along the dendrite to about 0.8 mV at the soma. Thus, synapses at S1 and S2 are predicted to have similar effects at the soma.

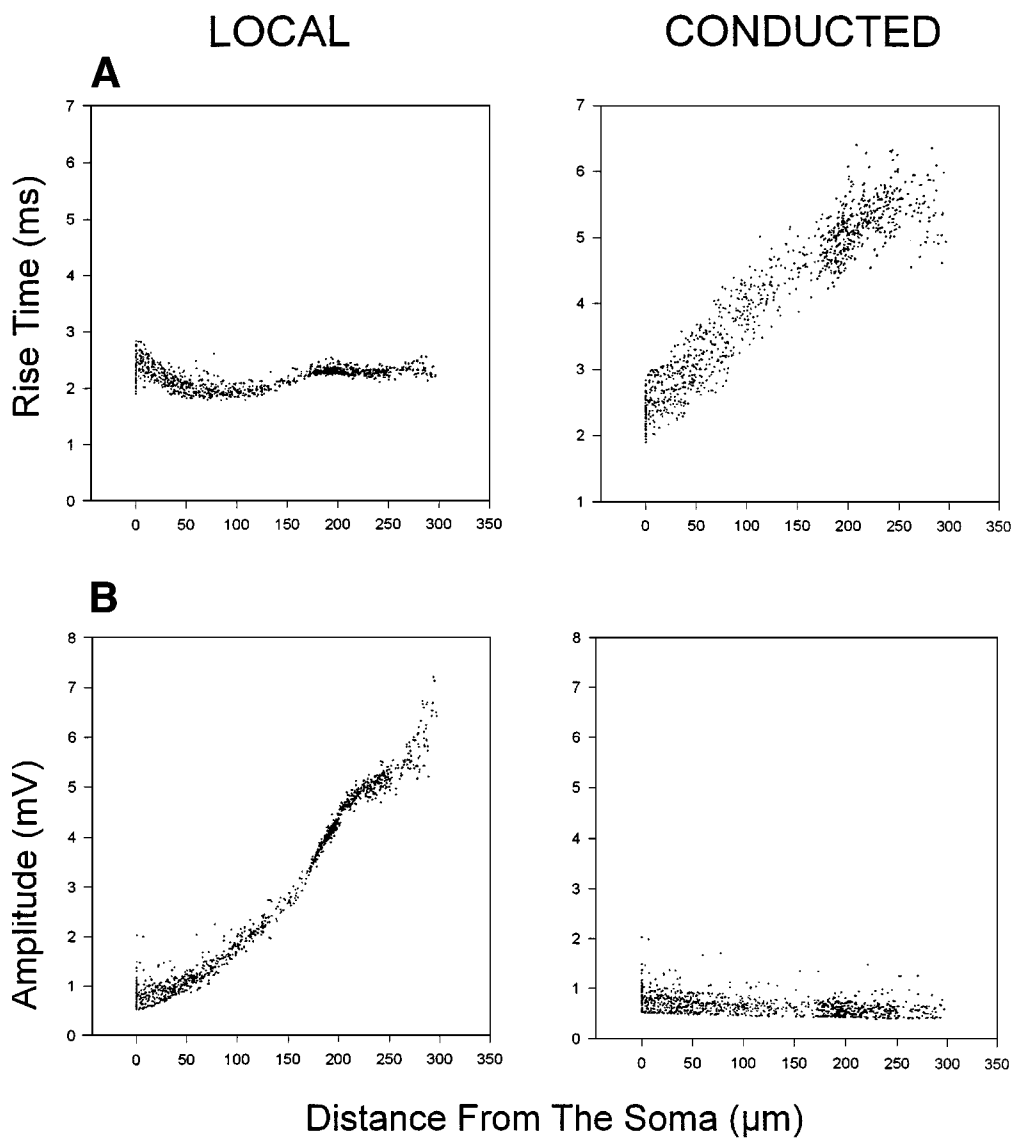

Figure 9. Comparison of simulated responses from different stochastically generated neurons, shown as response measurement versus distance from soma. For a given distance from the soma each data point is the simulated response from a different generated neuron. These results are from 1318 different synapse locations on 50 different generated neurons. A: Rise times (10–90%). B: Peak amplitudes of local and conducted responses. Each point represents the rise time or amplitude of the synapse-bearing shaft (local) or the soma (conducted) in response to a synapse located at the given distance—for example, 0 μm distance corresponds to a synapse on the soma and 300 μm corresponds to a synapse on a dendrite's distal tip at the hippocampal fissure. Same as in A and B but illustrating C population half-widths and D decay time (t_{dt}) of simulated local and conducted responses.

(*Continued on next page.*)

implications for the interpretation of the electrophysiologically recorded synaptic responses in the soma generated at different dendritic distances. Thus, one would expect that the rise times, but not the other parameters, show a clear dependence on the distance from the soma. This was indeed observed in the electrophysiological experiments, where we produced synaptic responses in LPP (distal) and MPP (proximal) segments of the dendritic trees. The variability due to shapes apparently masked the dependence on distances in the cases of half-amplitude and decay times (see table in Fig. 10). We were unable to compare the local simulated

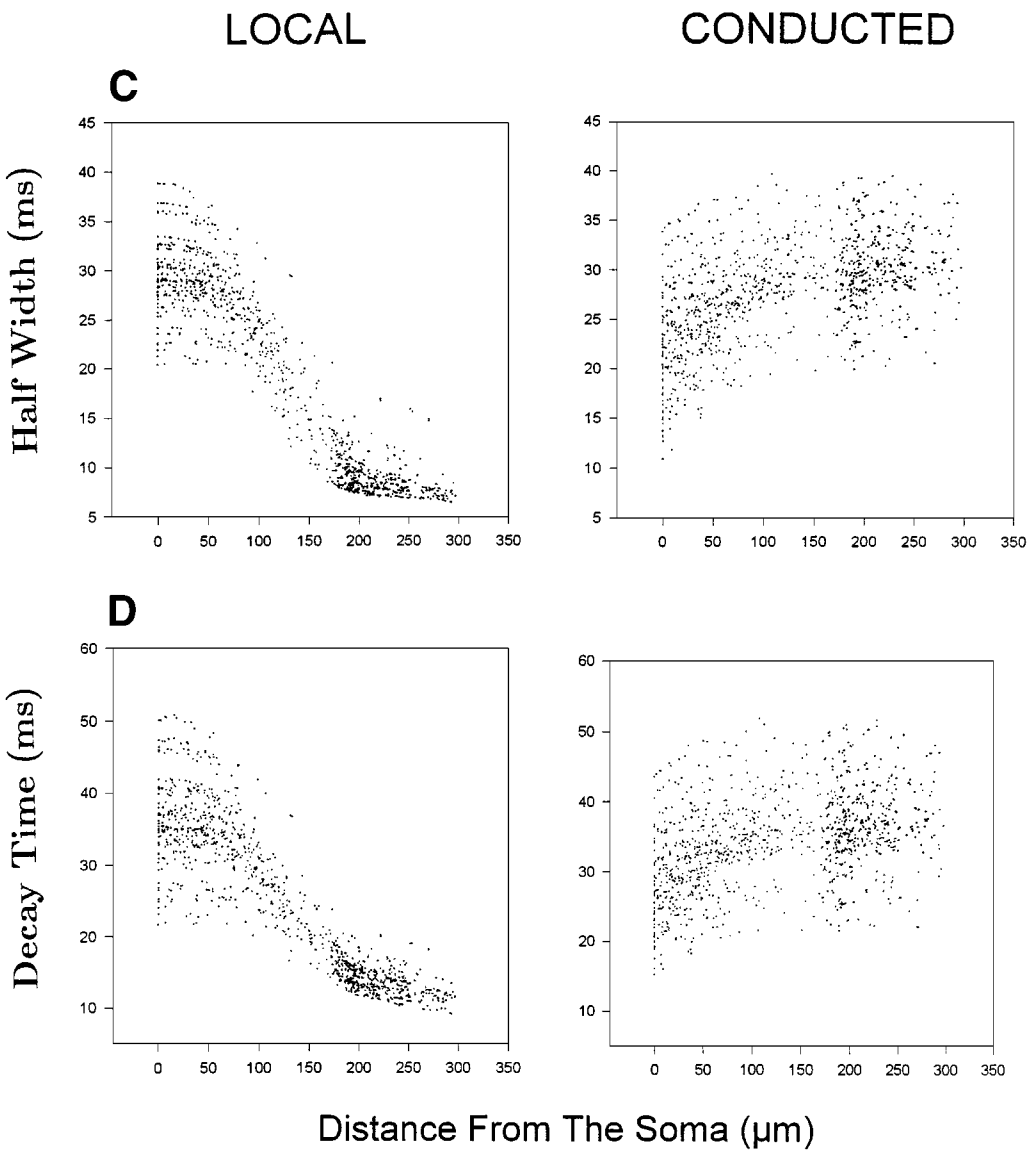

Figure 9. (*Continued*).

responses with the electrophysiological data because the dendritic recordings in these particularly thin dendrites are not presently feasible.

It should be noted that, at present, we are not certain how much of the variability in the parameter values is due to variations between different locations in a given shape and how much is due to differences in shapes. The experiments on a given shape could be easily performed on the modeled dendrites, as we have done in Figs. 7 and 8, for example. However, the electrophysiological verification of these results is not feasible, since, in the slice preparation, it is not possible to synaptically activate the exact known dendritic branch with any certainty. Such experiments are possible in cell culture, where the individual dendrites can be seen under a high-power microscope (see below, Section 4.3). The geometry of dendrites is, however, distorted in culture, due to abnormal growth conditions and the unavoidable two-dimensional arrangements of the branches.

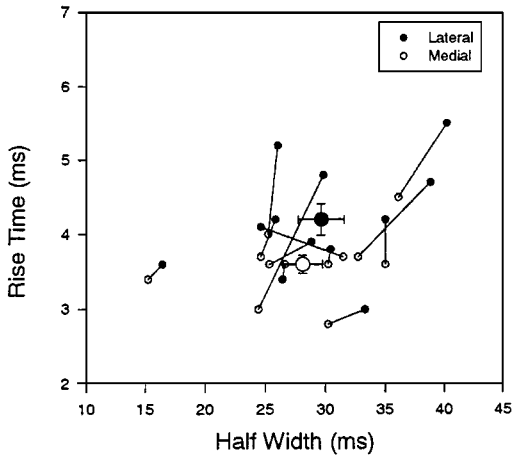

	Lateral	Medial
n	12	12
Amplitude (mV)	6.79±3.33	6.88±3.33
10-90% Rise Time (ms)	4.20±0.74*	3.60±0.43*
Half-Width (ms)	29.5±6.69	28.1±5.75
Decay Time, t_{dt} (ms)	33.1±7.81	31.6±7.56

Figure 10. Comparison of rise times and half-widths in depolarizing responses at lateral and medial synapses. Averaged evoked reponses were compared in 12 experiments. The mean values and their standard errors are shown by large symbols. The pairs of responses from LPP and MPP to the same neuron are joined by lines to indicate that in all but one case the rise times were longer in the lateral responses. The table below shows that the mean rise-time was significantly longer (*) in the lateral responses (paired t-test, $P < 0.05$).

The simulations on the population of stochastic neurons also appear to offer at least a partial explanation for the observed variation in the electrophysiologically reported values of input resistances (see Section 3.2). Our simulations show that a large part of this variation could be due to shapes. Thus, neurons with dendritic trees possessing single primary dendrites and relatively few proximal branches presumably yield relatively higher R_N values. This prediction can be examined in future electrophysiological and simulation experiments by comparing R_N values for each identified dendritic shape.

4.3. Physiological Implications of Signal Processing in Dendrites

All of the characteristics above apply only when the cell is behaving passively, as when responding to low-amplitude synaptic activations. Active mechanisms were not required to explain the shape characteristics of the responses to low-level activation. However, when larger evoked responses are recorded, the shapes of the resultant synaptic responses in DG granule neurons take on different characteristics. In particular, the half-widths are much smaller, and the responses fall more rapidly (data not shown), probably as a result of active, voltage-gated channels, which are opened by the large depolarizations.

Since different generated cell shapes were used, one can be reasonably confident that the general transmission properties observed may apply to the general population of DG granule cell geometries found *in vivo*. In addition, the variation in geometry may help to explain differences in R_m computed from R_N in the DG granule cell population. This could be a source of variation in other reported values of R_m in the literature.

The key feature of dentate gyrus is the convergence of LPP and MMP inputs on dendrites of granule neurons. The physiological consequences of this convergence are not known. In the hippocampal slice preparation, it can be shown that LPP can boost or increase long-term potentiation (LTP) in MPP when two inputs are coactivated (Wang and Wojtowicz, 1997). One way to explain this phenomenon arises from the characteristics of dendritic transmission described in this article. Since the distal region of the dendritic tree depolarizes much more than the medial region, the axial current will predominantly move in the distal to proximal direction during coactivation of the two pathways. As a result, the medial region will receive a large depolarization and consequently produce larger LTP.

The simulations suggest that it is difficult to distinguish the location of a synapse from its conducted, low-level soma response. The amplitude, half-width, and decay time of simulated conducted responses to MPP activation are not significantly different from those of simulated conducted responses to LPP activation (Table 6, and Fig. 9). It has been shown (e.g., Rall, 1964; Holmes, 1989) that the conducted response at the soma has longer rise times for distal compared with proximal synapses. For granule neurons, rise time is the best predictor of synapse location. This agreed with the analysis of actual cell responses recorded in DG granule neurons (compare with Fig. 10). Of the four response shape characteristics analyzed, only rise time appeared to be significantly correlated with synapse location.

The finding that the response due to input from LPP takes an extra 1 ms in rise time than MPP synapses in simulations could be critical for timing of the initiation of action potentials at the spike-generating site. This issue needs further experimental verification.

4.4. Comparison of Our Experiments with Others

The inability to easily discern synaptic origin from actual conducted responses in DG granule cells on the basis of their half-widths (Fig. 10) differs from experiments done in cat spinal motoneurons (Jack et al., 1971, 1975; Iansek and Redman, 1973), where plots of half-widths versus rise times formed an almost linear relationship with synapse distance. One possible reason for this is that the cat spinal motoneuron measurements were all made in a single fiber, whereas the experimental setup used here to selectively stimulate MPP and LPP synapses (Fig. 6) does not allow any control over which strand (or strands) within the dendritic tree is activated. Likewise, in our simulations, different branches were activated at random (Fig. 9, Table 6).

Pioneering experiments on pyramidal hippocampal neurons in CA1 showed no significant difference in rise time or half-width between distal and proximal inputs (Andersen et al., 1980). More recent measurements using the whole-cell recording technique suggest a significant degree of attenuation of the distal responses along dendrites (Bekkers and Stevens, 1996). Other studies suggest that synapses terminating on distal dendrites may compensate for their remote location by increased size or strength (Stricker et al., 1996; Liu and Tsien, 1995; Pierce and Mendell, 1993; Pettit et al., 1997).

4.5. Limitations

Although the simulations in the stochastic population of neurons appear to produce useful or at least testable predictions, some parameter values used to construct the model need to be better defined. Specifically, the dendritic diameters and the numbers of dendritic spines would benefit from more extensive experimental data not presently available (see Sections 2.5 and 2.6). The incorporation of active membrane properties, including calcium, potassium, and sodium voltage- and time-dependent channels, will be ultimately necessary. The simulations shown in Figs. 8 and 9 suggest that the apparently small synaptic responses recorded at the soma may arise from much larger (up to fivefold to tenfold) responses generated locally in the dendrites. It is presently unknown whether such responses can activate voltage dependent channels in granule neurons. More experimental data are needed in this regard.

4.6. Stochastic Neural Networks

In addition to simulation of the dentate gyrus granule neurons, one can forsee similar stochastic treatment of other neuronal types. For example, the dendritic trees of the CA3 pyramidal neurons have been well described (Traub and Miles, 1991). These neurons could possibly be simulated stochastically, and the interactions of the population of granule neurons and CA3 pyramidal neurons could be examined, taking the geometrical variations into account. Thus, statistics of shape can be used with statistics of signals (e.g., Cowan, 1972). We envisage that this type of modeling will extend the presently used techniques of neuronal modelling, where all neurons are assumed to have the exact same shape and properties.

Acknowledgments

We thank the reviewers and the editor for their penetrating comments, which substantially improved the article. We gratefully acknowledge Leo Marin and Priya Manjoo for their help with the electron micrographs and the measurement of dendritic diameters. This work was support in part by a M.R.C. Group grant to J. Martin Wojtowicz and an N.S.E.R.C grant to James L. Winslow.

Note

1. Three distances are used in this article: (1) z-distance along an axis parallel to the long axis of the dendritic tree, (2) cumulative distance between branch points of a dendritic tree, (straight line without wiggle), and (3) cumulative arc length with dendritic wiggle.

References

Andersen P, Silfvenius H, Sunberg SH, Sveen O (1980) A comparison of distal and proximal dendritic synapses on CA1 pyramids in guinea pig hippocampal slices in vitro. *J. Physiol. (Lond.)* 307:273–299.

Bekkers JM, Stevens CF (1996) Cable properties of cultured hippocampal neurons determined from sucrose-evoked miniature EPSCs. *J. Neurophysiol.* 75:1250–1255.

Benz R, Frölich P, Länuger P, Montal M (1975) Electrical capacity of black lipid film of lipid bilayers made from monolayers. *Biochem. Biophys. Acta* 394:323–334.

Borst A, Haag J (1996) The intrinsic electrophysiological characteristics of fly lobula plate tangential cells: I. Passive membrane properties. *J. Comput. Neurosci.* 3:313–336.

Claiborne BJ, Amaral DG, Cowan WM (1990) Quantitative, three-dimensional analysis of granule cell dendrites in the rat dentate gyrus. *J. Comp. Neurol.* 302:206–219.

Cook EP, Johnston D (1997) Active dendrites reduce location-dependent variability of synaptic input trains. *J. Neurophysiol.* 78:2116–2128.

Cotman C, Taylor D, Lynch G (1973) Ultrastructural changes in synapses in the dentate gyrus of the rat during development. *Brain Res.* 63:205–213.

Cowan J (1972) Stochastic models of neuroelectric activity. In: SA Rice, KF Freed, JC Light, eds. Statistical Mechanics: New Concepts, New Problems, New Applications. Proc. 6-th IUPAP Conf. Statistical Mechanics. University of Chicago Press, Chicago, IL. pp. 109–127.

Cowan WM, Stanfield BB, Kishi K (1980) The development of the dentate gyrus. *Current Topics in Develop. Biol.* 15:103–157.

Crain B, Cotman C, Taylor D, Lynch G (1973) A quantitative electron microscopic study of synaptogenesis in the dentate gyrus of the rat. *Brain Res.* 63:195–204.

de Schutter ED, Bower JM (1994a) An active membrane model of the cerebellar purkinje cell. I: Simulation of current clamps in slice. *J. Neurophysiol.* 71(1):375–400.

de Schutter E, Bower JM (1994b) An active membrane model of the cerebellar purkinje cell. II: Simulation of synaptic responses. *J. Neurophysiol.* 71(1):401–419.

Desmond NL, Levy WB (1984) Dendritic caliber and the three-two power relationship of dentate granule cells. *J. Comp. Neurol.* 227:589–596.

Desmond NL, Levy WB (1985) Granule cell dendritic spine density in the rat hippocampus varies with spine shape and location. *Neurosci. Letters* 54:219–224.

Fettiplace R, Andrews DM, Haydon DA (1971) The thickness, composition and structure of some lipid bilayers and natural membranes. *J. Membr. Biol.* 5:277–296.

Hama K, Arii T, Kosaka T (1989) Three-dimensional morphometrical study of dendritic spines of the granule cell in the rat dentate gyrus with hvem stereo images. *J. Electron Microscopy Technique* 12:80–87.

Harris KM, Stevens JK (1989) Dendritic spines of CA1 pyramidal cells in the rat hippocampus: Serial electron microscopy with reference to their biophysical characteristics. *J. Neurosci.* 9:2982–2997.

Hayat MA (1981) Principles and Techniques of Electron Microscopy: Biological Applications (2nd ed.), University Park Press, Baltimore, MD.

Haydon DA, Requena J, Urban BW (1980) Some effect of aliphatic hydrocarbons on the electrical capacity and ionic currents of the squid giant axon membrane. *J. Physiol. (Lond.)* 309:229–245.

Hines M (1984) Efficient computation of branched nerve equations. *Int. J. Biomed. Comput.* 15:69–76.

Hines M (1989) A program for simulation of nerve equations with branching geometries. *J. Physiol. (Lond.)* 117:500–544.

Holmes WR (1989) The role of dendritic diameters in maximizing the effectiveness of synaptic inputs. *Brain Res.* 478:127–137.

Holmes WR, Levy WB (1990) Insights into associative long-term potentiation from computational models of NMDA receptor-mediated calcium influx and intracellular calcium concentration changes. *J. Neurophysiol.* 63:1148–1168.

Holmes WR, Rall WR (1992) Electrotonic models of neuronal dendrites and single neuron computation. In T McKenna, J Davis, SF Zornetzer, eds. Single Neuron Computation. Academic Press, New York. pp. 7–25.

Iansek R, Redman SJ (1973) The amplitude, time course and charge of unitary excitatory post-synaptic potentials evoked in spinal motoneurone dendrites. *J. Physiol.* 234:665–688.

Jack JJB, Miller S, Porter R, Redman SJ (1971) The time course of minimal excitatory post-synaptic potentials evoked in spinal motoneurons by group Ia afferent fibres. *J. Physiol.* 215:321–352.

Jack JJB, Noble D, Tsien RW (1975) Electric Current Flow in Excitable Cells. Clarendon Press, Oxford.

Johnston D, Wu SM-S (1995) Foundations of Cellular Neurophysiology. MIT Press, Cambridge.

Jonas P, Major G, Sakmann B (1993) Quantal components of unitary EPSCs at the mossy fibre synapse on CA3 pyramidal cells of rat hippocampus. *J. Physiol.* 472:615–663.

Jou SF, Winslow JL, Wang S, Wojtowicz JM (1995) Families of generated hippocampal dentate granule shapes used to determine effects of location on synaptic response. *Society for Neurosci. Abstr.* 21:584.

Koch C, Zador A (1993) The function of dendritic spines: Devices subserving biochemical rather than electrical compartmentalization. *J. Neurosci.* 13:413–422.

Liu G, Tsien R (1995) Properties of synaptic transmission at single hippocampal synaptic boutons. *Nature* 375:404–408.

Major G (1992) The physiology, morphology and modelling of cortical pyramidal neurones. Ph.D. thesis, Oxford University.

Major G, Larkman AU, Jonas P, Sakmann B, Jack JJB (1994) Detailed passive cable models of whole-cell recorded CA3 pyramidal neurons in rat hippocampal slices. *J. Neurosci.* 14(8):4613–4638.

Manor Y, Rinzel J, Segev I, Yarom Y (1997) Low-amplitude oscillations in the inferior olive: A model based on electrical coupling of neurons with heterogeneous channel densities. *J. Neurophysiol.* 77(5):2736–52.

Nitzan R, Segev I, Yarom Y (1990) Voltage behavior along the irregular dendritic structure of morphologically and physiologically characterized vagal motoneurons in the guinea pig. *J. Neurophysiol.* 63(2):333–346.

Pettit DL, Wang SSH, Gee KR, Augustine GJ (1997) Chemical two-photon uncaging: A novel approach to mapping glutamate receptors. *Neuron* 19:465–471.

Pierce JP, Mendell LM (1993) Quantitative ultrastructure of Ia boutons in the ventral horn: Scaling and positional relationships. *J. Neurosci.* 13:4748–4763.

Press WH, Teukolsky SA, Vetterling WT, Flannery BP (1992) Numerical Recipes in C. Press Syndicate of the University of Cambridge, New York.

Rall W (1957) Membrane time constant of motoneurons. *Science* 126:454.

Rall W (1959) Branching dendritic trees and motoneuron membrane resistivity. *Exper. Neurol.* 1:491–527.

Rall W (1964) Theoretical significance of dendritic trees for neuronal input-output relations. In: RF Reiss, ed. Neural Theory and Modeling. Stanford University Press, Palo Alto, CA. pp. 73–97.

Rall W (1989) Cable theory for dendritic neurons. In: C Koch, I Segev, eds. Methods in Neuronal Modeling: From Synapses to Networks. MIT Press, Cambridge, MA. pp. 9–62.

Rall W, Burke RE, Holmes WR, Jack, JJB, Redman SJ, Segev I (1992) Matching dendritic neuron models to experimental data. *Physiol. Rev.* 72(4) (Suppl.):S159–S186.

Rall W, Rinzel J (1973) Branch input resistance and steady attenuation for input to one branch of a dendritic neuron model. *Biophys. J.* 13:648–688.

Rapp M, Segev I, Yarom Y (1994) Physiology, morphology and detailed passive models of guinea-pig cerebellar purkinje cells. *J. Physiol.* 474(1):101–118.

Segev I, Fleshman JW, Burke RE (1989) Compartmental models of complex neurons. In: C Koch, I Segev, eds. Methods in Neuronal Modeling: From Synapses to Networks. MIT Press, Cambridge, MA. pp. 63–96.

Segev I, Rapp M, Manor Y, Yarom Y (1992) Analog and digital processing in single nerve cells: Dendritic integration and axonal propagation. In: T McKenna, J Davis, SF Zornetzer, eds. Single Neuron Computation. Academic Press, New York. pp. 173–198.

Shelton DP (1985) Membrane resistivity estimated by means of a passive computer model. *Neurosci.* 14:111–131.

Spruston N, Jaffe DB, Johnston D (1994) Dendritic attenuation of synaptic potentials and currents: The role of passive membrane properties. *TINS* 17(4):161–166.

Spruston N, Jaffe DB, Williams SH, Johnston D (1993) Voltage- and space-clamp errors associated with the measurement of electrotonically remote synaptic events. *J. Neurophysiol.* 70(2):781–802.

Staley KJ, Otis TS, Mody I (1992) Membrane properties of dentate gyrus granule cells: Comparison of sharp microelectrode and whole-cell recordings. *J. Neurophysiol.* 67:1346–1358.

Stratford KA, Mason A, Larkman A, Major G, Jack JJB (1989) The modelling of pyramidal neurons in the visual cortex. In: R Durbin, C Miall, G Mitchison, eds. The Computing Neurons. Addison-Wesley, Reading, MA. pp. 296–321.

Stricker C, Field AC, Redman SJ (1996) Statistical analysis of amplitude fluctuations in EPSCs evoked in rat CA1 pyramidal neurones in vitro. *J. Physiol. (Lond.)* 490.2:419–441.

Stuart GJ, Sakmann B (1994) Active propagation of somatic action potentials into neocortical pyramidal cell dendrites. *Nature* 367:69–72.

Takashima S (1976) Membrane capacity of squid giant axon during hyper- and depolarisations. *J. Membr. Biol.* 27:21–39.

Takashima S, Schwan HP (1974) Passive electrical properties of squid axon membrane. *J. Membr. Biol.* 17:51–68.

Thurbon D, Field A, Redman S (1994) Electrotonic profiles of interneurons in stratum pyramidale of the CA1 region of rat hippocampus. *J. Neurophysiol.* 71(5):1948–1958.

Traub R, Miles R (1991) Neuronal Networks of the Hippocampus. Cambridge University Press, Cambridge.

Wang S, Wojtowicz JM (1997) Effect of $GABA_B$ receptors on synaptic interactions in dentate gyrus granule neurons of the rat. *Neurosci.* 79(1):117–127.

Wang S, Wojtowicz JM, Atwood HL (1996) Synaptic recruitment during long-term potentiation at synapses of the medial perforant pathway in the dentate gyrus of the rat brain. *Synapse* 22:78–86.

Wilson MA, Bower JM (1989) The simulation of large-scale neural networks. In: C Koch, I Segev, eds. Methods in Neural Modeling: From Synapses to Networks. MIT Press, Cambridge, MA. pp. 291–333.

Winslow JL (1990) Analysis and numerical solution of the dendrite equation with synapses applied to cochlear neurons. *Prog. Neurobiol.* 34:91–105.

Winslow JL (1994) Manual for WIN: A convenient video digitizing of NTSC, RS-170 or PAL video format. Physiology Department, University of Toronto, Toronto, Canada.

Winslow JL (1995) Tree: A neuron tree tracing program. Physiology Department, University of Toronto, Toronto, Canada.

Winslow JL, Bjerknes M, Cheng H (1987) Three-dimensional reconstruction of biological objects using a graphics engine. *Computers and Biomed. Res.* 20:583–602.

Witter MP (1993) Organization of the entorhinal-hippocampal system: A review of current anatomical data. *Hippocampus* 3 (special issue), 33–44.

Zhang L, Valiante TA, Carlen PL (1993) Contribution of the low-threshold T-type calcium current in generating the post-spike depolarizing afterpotential in dentate granule neurons of immature rats. *J. Neurophysiol.* 70(1):223–231.